

# Large spin-orbit splitting and weakly-anisotropic superconductivity revealed with single-crystalline noncentrosymmetric $\text{CaIrSi}_3$

G. Eguchi<sup>1,\*</sup>, H. Wadati<sup>2</sup>, T. Sugiyama<sup>3</sup>, E. Ikenaga<sup>4</sup>, S. Yonezawa<sup>1</sup>, and Y. Maeno<sup>1</sup>

<sup>1</sup>*Department of Physics, Graduate School of Science, Kyoto University, Kyoto 606-8502, Japan*

<sup>2</sup>*Department of Applied Physics and Quantum-Phase Electronics Center (QPEC),  
University of Tokyo, Hongo, Tokyo 113-8656, Japan*

<sup>3</sup>*Research Center for Synchrotron Light Applications, Kyushu University, Kasuga 816-8580, Japan*

<sup>4</sup>*Japan Synchrotron Radiation Research Institute (JASRI)/SPring-8, Kouto, Mikazuki 679-5198, Japan*

(Dated: August 22, 2012)

We report normal and superconducting properties of the Rashba-type noncentrosymmetric compound  $\text{CaIrSi}_3$ , using single crystalline samples with nearly 100% superconducting volume fraction. The electronic density of states revealed by the hard x-ray photoemission spectroscopy can be well explained by the relativistic first-principle band calculation. This indicates that strong spin-orbit interaction indeed affects the electronic states of this compound. The obtained  $H - T$  phase diagram exhibits only approximately 10% anisotropy, indicating that the superconducting properties are almost three dimensional. Nevertheless, strongly anisotropic vortex pinning is observed.

**PACS numbers:** 74.25.-q, 81.10.Dn, 79.60.-i, 71.20.Be

## I. INTRODUCTION

Superconductivity in the absence of inversion symmetry has been attracting much attention for its potential exotic superconducting phenomena [1, 2]. In bulk materials, such superconductivity is realized in crystals without inversion centers, namely in the so-called noncentrosymmetric superconductors (NCSCs) [3]. The lack of the inversion symmetry results in two important features. Firstly, the superconducting state cannot be classified either as a pure spin-singlet or a pure spin-triplet pairing any more, but is a singlet-triplet mixed pairing. Then, the superconducting gap function is generally expressed as  $\hat{\Delta}_{\mathbf{k}} = \{\Delta_1 \psi(\mathbf{k}) + \Delta_2 \mathbf{d}(\mathbf{k}) \cdot \hat{\sigma}\} i\hat{\sigma}_y$ . Here,  $\psi(\mathbf{k})$  and  $\mathbf{d}(\mathbf{k})$  are the normalized scalar superconducting gap function for the spin-singlet component and the normalized vector gap function for the spin-triplet component, respectively;  $\Delta_1$  and  $\Delta_2$  are the gap magnitudes, including  $\Delta_2 = 0$  (spin-singlet state) or  $\Delta_1 = 0$  (spin-triplet state) as special cases; and  $\hat{\sigma}$  is the Pauli matrices.

Secondly, the lack of inversion symmetry results in electronic energy-band splitting due to the antisymmetric spin-orbit interaction (ASOI). The ASOI term in the Hamiltonian is given by the inner product of the dimensionless  $g$ -vector  $\mathbf{g}(\mathbf{k})$  and the  $\mathbf{k}$ -dependent electron spin  $\boldsymbol{\sigma}(\mathbf{k})$ :  $H_{\text{ASOI}} = \alpha \Sigma_{\mathbf{k}} \mathbf{g}(\mathbf{k}) \cdot \boldsymbol{\sigma}(\mathbf{k})$ . Here  $\alpha$  characterizes the strength of the ASOI. The ASOI leads to an energy shift of  $\pm \alpha |\mathbf{g}(\mathbf{k})|$ , which can be interpreted as an effective  $\mathbf{k}$ -dependent Zeeman splitting of the electron spins [4]. It has been revealed that  $\mathbf{d}(\mathbf{k}) \parallel \mathbf{g}(\mathbf{k})$  is energetically favored for  $\alpha \gg |\Delta_{\mathbf{k}}|$ . Furthermore,  $\psi(\mathbf{k})$  and  $\mathbf{d}(\mathbf{k})$  belong to the same irreducible representation of the crystalline point group, and  $\mathbf{d}(\mathbf{k})$  is expressed as  $\mathbf{d}(\mathbf{k}) = \psi(\mathbf{k}) \mathbf{g}(\mathbf{k})$  [5, 6]. This indicates

that the superconducting energy gap  $\Delta_{\mathbf{k}\pm}$  takes the form  $\Delta_{\mathbf{k}\pm} = \psi(\mathbf{k}) \{\Delta_1 \pm \Delta_2 |\mathbf{g}(\mathbf{k})|\}$  on each split energy band.

One of the typical and well-studied ASOIs is of the Rashba-type, whose  $g$ -vector has the form  $\mathbf{g}(\mathbf{k}) \propto (k_y, -k_x, 0)$  [2]. Because of this simple form, NCSCs having the Rashba-type ASOI are favorable for the investigation of the novel superconducting state. In fact, a number of unusual superconducting phenomena originating from the parity mixing or the ASOI have been proposed: e.g., helical vortex state and novel magnetoelectric effect [4, 7]. For observation of any of such phenomena, single crystalline sample is crucially important, because the novel effects are likely to be canceled out in polycrystals.

Naively speaking, the Rashba-type ASOI is expected to be realized in crystals in which inversion symmetry is broken only along one direction. To our knowledge, only seven Rashba-type NCSCs with single crystals are reported up until today:  $R\text{Pt}_3\text{Si}$  ( $R=\text{La, Ce}$ ) [8, 9],  $R\text{RhSi}_3$  and  $R\text{IrSi}_3$  ( $R=\text{La, Ce}$ ) [10–12], and  $\text{CeCoGe}_3$  [13]. The four Ce-based NCSCs indeed exhibit exotic superconducting behavior. However, they also exhibit antiferromagnetic ordering in the vicinity of the superconducting phase. Thus, it is difficult to distinguish effects originating from the ASOI from effects resulting from active  $f$ -electrons. In contrast, the other three La-based NCSCs exhibit conventional metallic behavior in their normal states and weak-coupling full-gap behavior in their superconducting states. This fact may suggest importance of the active  $f$ -electrons for realization of the novel phenomena. However, a few NCSCs having different crystal structures indeed exhibit novel superconducting phenomena, even though active  $f$ -electrons are not present [14, 15]. Thus, further investigations of nonmagnetic,  $f$ -electron-free Rashba-type NCSCs are important.

Here, we report our success in growing single crystals of the Ca-based NCSC  $\text{CaIrSi}_3$ , which has the

\* geguchi@scphys.kyoto-u.ac.jp

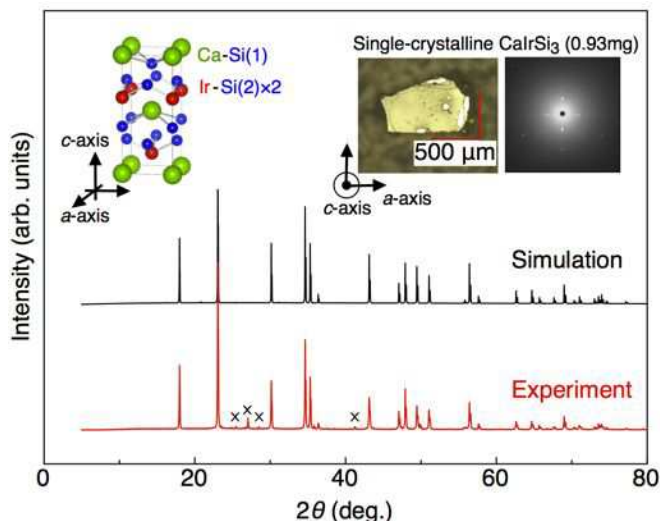


FIG. 1. (Color online) Experimental and simulated powder x-ray diffraction spectra of  $\text{CaIrSi}_3$ . The small impurity peaks indicated by  $\times$  marks are attributed to a by-product  $\text{CaIr}_3\text{Si}_7$  [17], whose grains are distinct from  $\text{CaIrSi}_3$  crystals. The upper-left inset illustrates the crystal structure of  $\text{CaIrSi}_3$ . This schematic was produced by the software VESTA [20]. A optical microscope picture of a single crystal and its backscattered Laue photograph are also shown in the upper-right inset.

same crystal structure as  $R\text{IrSi}_3$  ( $R=\text{La}, \text{Ce}$ ).  $\text{CaIrSi}_3$  exhibits superconductivity below the critical temperature  $T_c = 3.6 \text{ K}$  [16], which is the highest  $T_c$  among the known Rashba-type NCSCs. We previously reported that  $\text{CaIrSi}_3$  is a non-magnetic, fully-gapped superconductor based on studies with polycrystalline samples [17, 18]. Single crystalline samples allow examinations of various predicted exotic phenomena as well as investigation of basic information of superconductivity, such as the gap anisotropy and the mixing ratio of the singlet and triplet components. In this paper, we describe the synthesis of single crystalline  $\text{CaIrSi}_3$ , and its normal and superconducting properties. We also present the electronic density of states (DOS) near the Fermi energy  $E_F$  revealed by bulk sensitive hard x-ray photoemission spectroscopy (HAXPES), and by relativistic first-principle calculations [19]. By comparing the results of HAXPES and the band calculations, we revealed existence of strong SOI in this material. The compound can be a model material having strong SOI with  $5d$  orbital characters.

## II. SINGLE CRYSTAL GROWTH

Single crystalline  $\text{CaIrSi}_3$  is synthesized by a combination of the arc melting [17] and self-flux methods. Firstly, polycrystalline  $\text{CaIrSi}_3$  was obtained by the arc melting of a pellet made of a powder mixture of  $\text{CaSi}$  (99.9%),  $\text{Ir}$  (99.99%), and  $\text{Si}$  (99.999%) with the molar

ratio  $\text{Ca}:\text{Ir}:\text{Si} = 3:1:4.7$ . Secondly, small single crystalline grains of  $\text{CaIrSi}_3$  were isolated by dissolving a by-product  $\text{CaSi}_x$  into 3% hydrochloric acid. Thirdly, these grains were mixed with a sufficient amount, typically twenty times of the Ir-molar mass of the grains, of the  $\text{CaSi}$ ,  $\text{Ir}$ , and  $\text{Si}$  powders with the molar ratio  $\text{Ca}:\text{Ir}:\text{Si} = 3:1:4.7$  in Ar atmosphere, then pressed into a pellet. The pellet was put into an alumina crucible, which was then capsulated into a stainless steel container in an Ar atmosphere [21]. The container was heated up to  $1340^\circ\text{C}$ , cooled to  $800^\circ\text{C}$  by  $2^\circ\text{C/h}$ , then quenched. Many pieces of single crystalline  $\text{CaIrSi}_3$  with the size  $0.2\text{-}1.4 \text{ mm}$  are obtained along with a slight amount of by-product  $\text{CaIr}_3\text{Si}_7$ .

A powder x-ray diffraction spectrum (Bruker AXS D8 ADVANCE) of crushed single crystals is presented in Fig. 1. The obtained spectrum well agrees with the simulation. An optical microscope picture of a crystal with the typical size of  $0.5 \times 0.5 \times 0.5 \text{ mm}^3$  is presented in the upper-right inset. A backscattered Laue photograph of the presented crystal is also shown. This photograph was taken with an apparatus (RIGAKU RASCO-BLII) in which a charge-coupled-device (CCD) camera takes the image of a Laue pattern projected onto a fluorescent screen. The clear four-fold symmetry in the Laue picture indicates that the surface shown corresponds to the basal  $ab$  plane.

## III. HARD X-RAY PHOTOEMISSION SPECTRUM

A photoemission spectrum around  $E_F$  revealed by the bulk sensitive HAXPES is presented in Fig. 2(a). The measurement was performed at the beamline BL47XU at SPring-8 (Japan) [22]. The setup of the measurement is depicted in the inset: incident photons with an energy of  $7.9399 \text{ keV}$  have their polarization plane perpendicular to the sample surface. The DOS deduced from the full potential linearize augmented plane wave (FLAPW) calculation performed by WIEN2k package with/without SOI are presented in Fig. 2(b) together with the partial DOS for each atom. Our calculation well reproduces the previous calculation in Ref. [23]. From the DOS, we simulate the HAXPES spectrum by assuming a Lorentzian-type lifetime broadening with the energy-dependent line width ( $\text{FWHM}=0.2|E - E_F|$ ) [24], and compared it in Fig. 2(c) with the background-subtracted experimental spectrum. The calculation with the SOI explains the experimental result better than that without the SOI: In particular, the shoulder-like structure at approximately  $3 \text{ eV}$  for the latter is absent in the experimental spectrum. The fact indicates that strong SOI indeed affects the electronic state of  $\text{CaIrSi}_3$ .

The calculated band dispersions with/without the SOI are shown in Fig. 2(d). The four-fold degeneracy at the symmetric  $\Gamma$  point is split into two by  $\sim 0.42 \text{ eV}$  due to the SOI. Note that this energy split at the  $\Gamma$  point ( $\mathbf{k} = 0$ ) is caused by the symmetric SOI, which

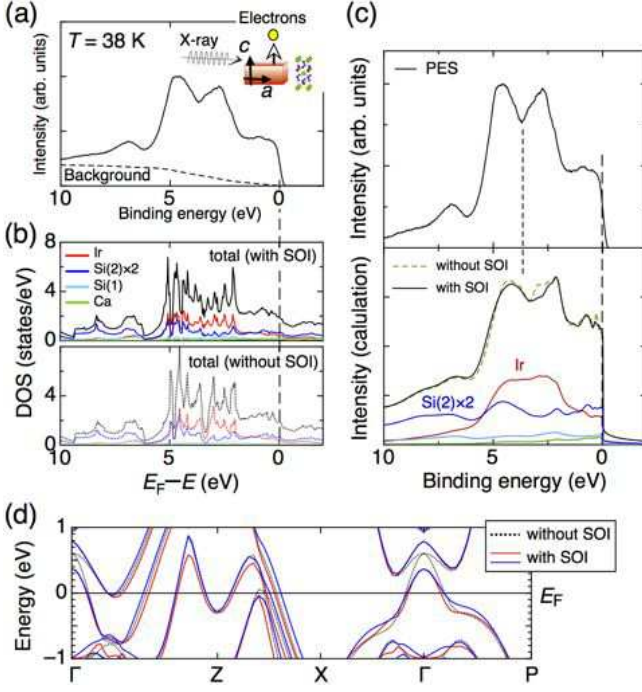


FIG. 2. (Color online) (a) Photoemission spectrum near  $E_F$ . A schematic of the experimental setup is presented in the inset. (b) Calculated DOS of  $\text{CaIrSi}_3$  by the local density approximation (LDA) band calculation with and without spin-orbit interaction (SOI). Partial DOS for each atom is also presented. (c) Comparison between the background-subtracted experimental spectrum and the calculated spectrum with an assumed life-time broadening. The calculation with SOI well describes the experimental result than that without SOI does. Contribution of each atom to the spectrum is also presented based on the calculation with SOI. (d) Band dispersion with/without SOI. Spin-orbit splitting of the two-fold spin degeneracy near  $E_F$  is  $0.05 \sim 0.3$  eV.

can be finite regardless of the crystal symmetry. The value of the  $\Gamma$ -point splitting is consistent with a previous study [23]. The value is also comparable to that of  $\text{CeIrSi}_3$ : 0.4 eV [25], in which Ce  $4f$  orbitals dominantly contribute to the electronic conduction. The remaining two-fold spin degeneracy is split by  $\sim 0.05\text{--}0.3$  eV at less symmetric  $k$  points due to the ASOI. The band splitting results in approximately 10% DOS difference ( $\delta N \sim 0.1$ ) between the ASOI-split Fermi surfaces. As presented in Figs. 2(b)(c), the Ir- $5d$  orbital contributes by 20-50% to the total DOS near  $E_F$ . Thus, the influence of the strong SOI discussed above is attributed to the Ir orbitals.

#### IV. NORMAL-STATE AND SUPERCONDUCTING PROPERTIES

The temperature dependence of the resistivity  $\rho$  is presented in Fig. 3(a), while the low temperature  $\rho$  and specific heat  $c_p$  of the same sample are presented in Fig. 3(b). The measurements were performed with a

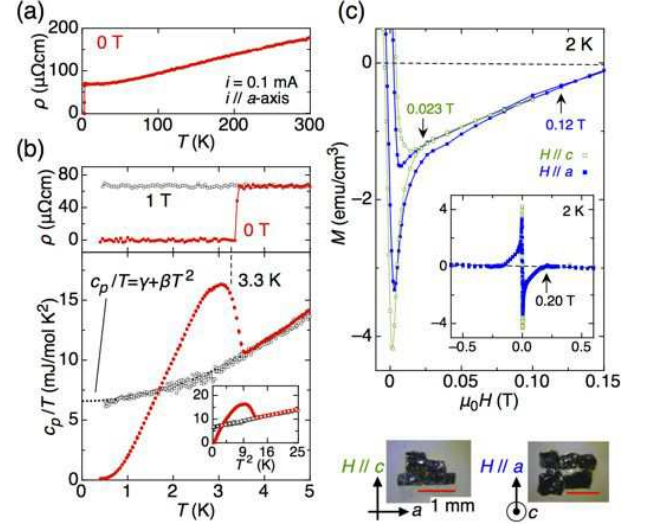


FIG. 3. (Color online) (a) Temperature dependence of the resistivity  $\rho$  of the single crystalline  $\text{CaIrSi}_3$ . (b) Low-temperature resistivity and specific heat divided by temperature,  $c_p/T$ , at 0 T and 1 T ( $H \parallel a$ ). The broken vertical line indicates  $T_c = 3.3$  K based on the entropy conservation. The inset is a  $c_p/T$ -vs- $T^2$  plot, indicating that the relation  $c_p/T = \gamma + \beta T^2$  well describes the normal-state behavior. (c) Magnetization  $M$  vs. external field  $H$  curves at 2 K for  $H \parallel a$  axis (filled symbols) and  $H \parallel c$  axis (open symbols). The irreversibility field for each field direction is indicated by arrows. The inset is the full  $M - H$  curves. The dotted line with a slight negative slope represents the normal state diamagnetism. The onset of the magnetic shielding is 0.2 T at 2 K for both field directions. The measurement setups of the samples are also presented.

commercial apparatus (Quantum Design PPMS) down to 0.35 K with a  $^3\text{He}$  refrigerator. For the specific heat measurements, three crystals from the same batch were added to achieve sufficient experimental resolution (total: 7.301 mg). Their crystal axes were determined individually by the Laue photography. The onset temperature of the specific-heat jump in zero field is 3.55 K, which is consistent with the results for polycrystalline samples [17]. The thermodynamic  $T_c$  determined by the entropy conservation criteria, is 3.3 K. The superconductivity is suppressed by a field of 1 T ( $H \parallel a$ ). Both the specific heat and resistivity in the normal state are magnetic-field independent within the experimental resolutions. The residual resistivity  $\rho_0$  of the present sample is  $68 \mu\Omega\text{cm}$ . The residual resistivity ratio  $RRR \equiv \rho(300 \text{ K})/\rho(5 \text{ K})$  is 2.6. Both  $\rho_0$  and  $RRR$  are comparable to that of polycrystalline samples [17].

The normal state  $c_p$  below 5 K is well described by the conventional Debye-Sommerfeld model:  $c_p = \gamma T + \beta T^3$ , where  $\gamma$  is the electronic specific heat coefficient and  $\beta$  is the phononic specific heat coefficient. We obtain  $\gamma = 6.6 \text{ mJ/mol K}^2$  and  $\beta = 0.31 \text{ mJ/mol K}^4$  from the fitting to the normal state data between 0.35 and 5 K. The Debye temperature  $\Theta_D$  calculated

from  $\beta = (12/5)\pi^4 N_A N_{f.u.} k_B / \Theta_D^3$  is 314 K. Here,  $N_A$  is the Avogadro number,  $N_{f.u.} = 5$  is the number of atoms per formula unit, and  $k_B$  is the Boltzmann constant. We obtain the electron-phonon coupling constant  $\lambda_{el-ph}$  as 0.56 from the McMillan's formula  $T_c = (\Theta_D/1.45)\exp[-1.04(1 + \lambda_{el-ph})/\{\lambda_{el-ph} - \mu^*(1 + 0.62\lambda_{el-ph})\}]$  [26] with  $\Theta_D = 314$  K and the Coulomb pseudo potential  $\mu^* = 0.13$ . The obtained small value of  $\lambda_{el-ph}$  indicates that a weak-coupling superconductivity is realized in this compound, being consistent with the specific heat described below. The DOS from our calculation provides  $\gamma_0 = 2.3$  mJ/molK<sup>2</sup>, yielding the electronic mass-enhancement factor  $\gamma/\gamma_0 = 2.9$ . This value is larger than that of pure Ir metal: 1.3 [27, 28].

The superconducting  $M-H$  curves at 2 K for dc magnetic fields  $H \parallel c$  and  $H \parallel a$  are presented in Fig. 3(c). The measurements were performed with a commercial magnetometer (Quantum Design MPMS-XL). Photos of the experimental setups are presented at the bottom of Fig. 3(c); we arranged the crystals so that the difference of demagnetization factors between the measurements is small. Indeed, the difference in their superconducting magnetic shielding in the Meissner state is less than 30%. The inset is the whole  $M-H$  loops, indicating that the magnetic shielding occurs below  $\pm 0.20$  T for both field directions. The loops exhibit typical behavior of type-II superconductivity with weak vortex pinning. As presented in the figure, the irreversible field is 0.12 T for  $H \parallel a$ , and 0.023 T for  $H \parallel c$ . This anisotropic behavior indicates that vortex pinning for  $H \parallel a$  is stronger than that for  $H \parallel c$ . Such anisotropic pinning was reproducibly observed in other measurements with a single piece of a crystal from the same batch and with several pieces of crystals from another batch. The negative slope of  $M$  vs.  $H$  in the normal state shown in the inset of Fig. 3(c) indicates that CaIrSi<sub>3</sub> is a diamagnet. No anisotropy in the normal state was observed within the experimental resolution. The normal-state dc susceptibility  $\chi_{dc} = M/H$ , which is determined by another measurement with many single crystals without alignment of the crystal direction, is  $-1.1 \times 10^{-4}$  emu/mol. This value was almost invariant within the ranges  $\pm 7$  T and 2-300 K. The Pauli paramagnetic susceptibility of CaIrSi<sub>3</sub> estimated from the band calculations is  $\chi_P = 0.61 \times 10^{-4}$  emu/mol. The observed diamagnetism is attributable to the dominance of the core diamagnetism.

The temperature dependence of the electronic specific heat divided by temperature  $c_{el}/T = c_p/T - \beta T^2$  in several fields are presented in Fig. 4(a). The measurements for  $H \parallel a$  and  $H \parallel c$  were performed using the same crystals. At 0 T, the residual term of  $c_{el}/T$  for  $T \rightarrow 0$  is almost absent, indicating that the superconducting volume fraction is nearly 100% for these samples. The thermodynamic critical field  $\mu_0 H_c(0)$  evaluated from the relation  $\mu_0 H_c^2(0)/2 = -\gamma T_c^2/2 + \int_0^{T_c} c_{el}(T)dT$  is 0.028 T. The theoretical  $c_{el}/T$  based on the weak-coupling BCS model [29] presented in the figure well reproduces the observed temperature dependence below 2.7 K. The agreement indi-

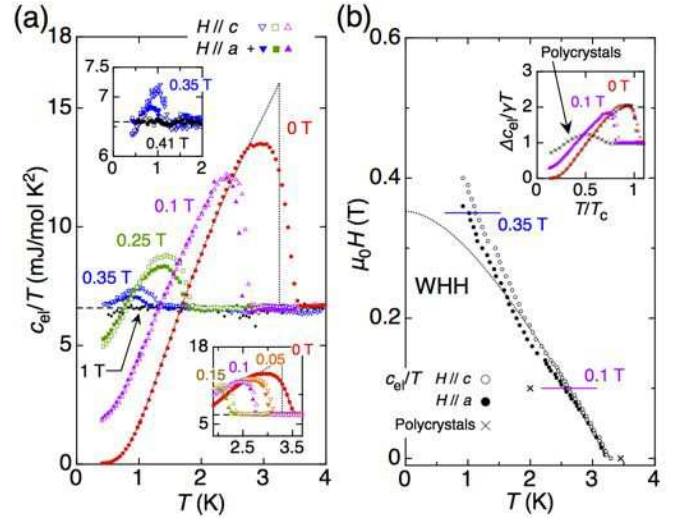


FIG. 4. (Color online) (a) Temperature dependence of the electronic specific heat divided by temperature,  $c_{el}/T$  for  $H \parallel a$  (closed symbols) and for  $H \parallel c$  (open symbols). The detailed  $c_{el}/T$  around 0.1 T and 0.4 T are presented in the insets. (b) Superconducting  $H-T$  phase diagram based on the thermodynamic  $T_c$  for  $H \parallel a$  (filled symbols) and  $H \parallel c$  (open symbols). The thermodynamic  $T_c$  of the polycrystalline sample [17] is also presented. The inset shows the comparison of the normalized  $\Delta c_{el}/\gamma T$  vs.  $T/T_c$  for the single crystal and the polycrystals at 0 and 0.1 T [17]. For the polycrystalline data,  $\gamma$  has been corrected for the residual  $c_{el}/T$  at 0 T (such  $\gamma$  is denoted as  $\gamma_s$  in Fig. 5 of [17]).

cates that the superconducting gap is finite on the entire Fermi surface. The deviation of the experimental data from the BCS curve above 2.7 K seems to be attributed to a  $T_c$  distribution within the samples. However, we will point out two tendencies opposite to the ordinary behavior. As presented in the lower inset of Fig. 3(a), the transition in 0 T is broader than that in 0.1 T. This is observed with another measurement with single crystalline samples from different batch (not shown). In addition, the specific-heat jump for the single crystals in 0 T is broader than that for polycrystals, as shown in the comparison of normalized  $\Delta c_{el}/\gamma T$  between the single crystal and the polycrystals in the inset of Fig. 4(b). These features will be discussed again in the next section. Note that the sharpening of the specific-heat jump in 0.1 T is not observed in polycrystals, probably due to the presence of the grain boundaries in polycrystals.

As presented in the upper inset of Fig. 3(a), the specific heat jump is visible in 0.35 T but not in 0.41 T for both field directions. The lower limit of the Ginzburg-Landau parameter  $\kappa_{GL}$  estimated from  $\mu_0 H_{c2}^{\parallel a} = 0.375$  T is 9.4, using the relation  $\kappa = H_{c2}^{\parallel a}/(\sqrt{2}H_c)$ . This lower limit is consistent with that of the polycrystals [17].

The  $H-T$  phase diagram deduced from the thermodynamic  $T_c$  for each field direction is presented in Fig. 4(b). For comparison, the thermodynamic  $T_c$  of polycrystals evaluated from the data reported in Ref. [17]



are also presented. The conventional Werthamer-Helfand-Hohenberg (WHH) curve for the upper critical field  $H_{c2}(T)$  in the dirty limit, giving  $\mu_0 H_{c2}^{\text{WHH}}(0) = -0.693 T_c [d(\mu_0 H_{c2})/dT]|_{T=T_c} = 0.35$  T, is also presented [30]. The WHH curve well agrees with the experimental result for  $H \parallel c$  above 2 K. However, the observed  $H_{c2}$  becomes substantially larger than  $\mu_0 H_{c2}^{\text{WHH}}(T)$  at lower temperatures for both field directions. In addition,  $H_{c2}$  for the  $c$  direction is higher than that for the  $a$  direction. This is also evident in the specific-heat data in Fig. 4(a). The ratio  $H_{c2}^{\parallel c}/H_{c2}^{\parallel a}(T)$  is approximately 1.1, which is almost invariant below 3 K. Such small anisotropy indicates a nearly three-dimensional superconducting nature.

## V. DISCUSSION

According to the group theory, the superconducting gap symmetry of CaIrSi<sub>3</sub> belongs to the  $C_{4v}$  point group, which is the same as that of CePt<sub>3</sub>Si [5]. There are five possible superconducting pairing symmetries allowed for this point group. The observed fully-gapped behavior indicates that the most symmetric  $A_1$  state with  $\Delta_1 > \Delta_2$  is realized, because this is the only case having a fully-gapped superconducting energy gap function. The gap function of the  $A_1$  state with the Rashba-type ASOI is expressed as  $\Delta_{\pm}(\theta_{\mathbf{k}}) = \Delta_1 \pm \Delta_2 \sin \theta_{\mathbf{k}}$  for the pair of ASOI-split bands. Here  $\theta_{\mathbf{k}}$  is the angle between the  $c$  axis and  $\mathbf{k}$ . Note that the superconductivity becomes multi-gapped if  $\Delta_2$  is finite.

As mentioned above, the superconducting transition at 0 T is broader than that at 0.1 T. Furthermore, the observed  $H - T$  curves deviate from the conventional WHH curve below 2 K. These feature may well be explained as a result of a distribution in both  $T_c$  and  $H_{c2}$ . In fact, the observed behavior is reproducible by assuming a two- $T_c$  BCS model, having one domain with lower  $T_c$  and higher  $H_{c2}$ , and another domain with higher  $T_c$  and lower  $H_{c2}$ . On the other hand, the observed behavior can be also explained as a result of multi-gapped superconductivity with small  $T_c$  distribution. In the present case, there are two possible multi-gapped superconductivity: one originating from multiple Fermi surfaces, or one from a finite  $\Delta_2$ . A high-resolution photoemission spectroscopy or a scanning tunneling spectroscopy in the superconducting state would give crucial indications.

Another interesting feature in the observed superconducting behavior is the anisotropic pinning observed in the  $M - H$  curves: the irreversible field at 2 K for  $H \parallel a$  is approximately five times larger than that for  $H \parallel c$ . Such anisotropic behavior cannot be explained by a simple pinning model with random defects and impurities. Thus, the anisotropic vortex pinning probably indicate an anisotropic distribution of lattice imperfections. CaIrSi<sub>3</sub> can have twin boundaries of crystalline domains with opposite directions of the Rashba field, as discussed in CePt<sub>3</sub>Si [31]. Such twin boundaries would

run both perpendicular to an in-plane axis and perpendicular to the  $c$ -axis. The anisotropic pinning may be caused by these twin boundaries. Note that novel vortex behavior occurring at the twin boundary, i.e., a fractional vortex, is discussed for CePt<sub>3</sub>Si for  $H \parallel a$ , in order to explain the observed extremely slow vortex dynamics [32]. Such interesting vortex phenomena might be related to the observed anisotropic pinning in CaIrSi<sub>3</sub>.

It has been theoretically predicted that the helical vortex state, which is unique to NCSCs, can be stable in the presence of finite  $\delta N$  [2, 4]. The helical vortex state has a superconducting gap function  $\Delta(\mathbf{r}) = |\Delta| e^{i\mathbf{q}_h \cdot \mathbf{r}}$  with  $\mathbf{q}_h \propto \hat{c} \times \mathbf{H}$ . This is analogous to the Fulde-Ferrell (FF) state [33], which exhibits a spatial phase modulation of  $\Delta(\mathbf{r})$ . Note that the finite  $\mathbf{q}_h$  originates from the asymmetric distortion of a Fermi surface induced by  $H$ , while the finite  $\mathbf{q}_{\text{FF}}$  of the FF state originates from the electron pairing between the Zeeman-split energy bands. For another difference, the helical vortex state can be realized down to near  $H = 0$  whereas the FF state can be stable only in high fields near the Pauli-limiting field  $H_P$ . For the helical vortex state, an enhancement of low-temperature  $H_{c2}$  associated with the emergence of a spatially modulated superconducting gap amplitude, or modulated vortex states, are discussed near  $H_P$  [2, 34]. However, this is not relevant to the case of CaIrSi<sub>3</sub> because  $\mu_0 H_P(0) \sim 6$  T is sufficiently larger than the actual  $H_{c2}$ . Here,  $\mu_0 H_P(0)$  is estimated from the relation  $\mu_0 H_P(0)/T_c = 1.84$  T/K. Nevertheless, other signatures related to the helical vortex state may be observed in CaIrSi<sub>3</sub>. For example, the observed  $H_{c2}$  enhancement in low temperatures is possibly related to properties of the helical vortex state at  $H \ll H_P$ . As well as the sample improvement, further investigation especially in the lower temperature region is necessary.

## VI. SUMMARY

We revealed the existence of strong SOI on CaIrSi<sub>3</sub> by HAXPES, and the nearly three-dimensional, fully gapped superconducting nature with anisotropic vortex pinning, using single crystalline samples. The physical properties evaluated in this study is summarized in the Table I. We emphasize that CaIrSi<sub>3</sub> is one of the simplest Rashba-type NCSC having strong SOI without active  $f$ -electrons. It is expected that the single crystalline samples would provide unique opportunities for investigations of novel superconducting phenomena related to the lack of the inversion symmetry.

## ACKNOWLEDGMENTS

We thank T. Matsuda, H. Ikeda, Y. Yanase, S. Fujimoto, D.C. Peets, M. Kriener, F. Kneidinger, and E. Bauer for fruitful discussions. This work is supported by a Grant-in-Aid for the Global COE program “The

TABLE I. Physical properties of  $\text{CaIrSi}_3$  obtained by this study. Here  $\gamma$  is the electronic specific heat coefficient,  $\Theta_D$  is the Debye temperature,  $T_c$  is the thermodynamic superconducting transition temperature,  $\mu_0 H_c(0)$  is the thermodynamic critical field,  $\lambda_{\text{el-ph}}$  is the electron-phonon coupling constant,  $\chi_{\text{dc}}$  is the dc magnetic susceptibility,  $E_F$  is the Fermi energy,  $N(E_F)$  is the density of states,  $\chi_P$  is the Pauli paramagnetic susceptibility, and  $n$  is the carrier density. The latter four values are obtained from the relativistic first principle calculations.

$\gamma$	6.6 mJ/mol K <sup>2</sup>
$\Theta_D$	314 K
$T_c$	3.3 K
$\mu_0 H_c(0)$	0.028 T
$\lambda_{\text{el-ph}}$	0.56
$\chi_{\text{dc}}$	$-1.1 \times 10^{-4}$ emu/mol
$\mu_0 H_{c2}^{\parallel a}$ (at 0.9 K)	0.375 T
$\kappa_{\text{GL}}$ (at 0.9 K)	9.4
$E_F$	8.26 eV
$N(E_F)$	1.93 states/eV
$\chi_P$	$0.61 \times 10^{-4}$ emu/mol
$n$	$1.6 \times 10^{23}$ /cm <sup>3</sup>

Next Generation of Physics, Spun from Universality and Emergence” from the Ministry of Education, Culture, Sports, Science, and Technology (MEXT) of Japan, and by the “Topological Quantum Phenomena” Grant-in Aid for Scientific Research on innovative Areas from MEXT of Japan, and by the Japan Society for the Promotion of Science (JSPS) through the “Funding Program for World Leading Innovative R&D on Science and Technology (FIRST Program)”, initiated by the Council for Science and Technology Policy (CSTP). The synchrotron radiation experiments at SPring-8 were performed under the approvals of the Japan Synchrotron Radiation Research Institute (2011B1710 and 2012A1624). G.E. is also supported by JSPS.

- [1] L. P. Gor'kov and E. I. Rashba, Phys. Rev. Lett. **87**, 037004 (2001).
- [2] D. F. Agterberg and R. P. Kaur, Phys. Rev. B **75**, 064511 (2007).
- [3] E. Bauer, G. Hilscher, H. Michor, C. Paul, E. W. Scheidt, A. Griбанov, Y. Seropegin, H. Noël, M. Sigríst, and P. Rogl, Phys. Rev. Lett. **92**, 027003 (2004).
- [4] R. P. Kaur, D. F. Agterberg, and M. Sigríst, Phys. Rev. Lett. **94**, 137002 (2005).
- [5] M. Sigríst, D. Agterberg, P. Frigeri, N. Hayashi, R. Kaur, A. Koga, I. Milat, K. Wakabayashi, and Y. Yanase, J. Magn. Magn. Mat. **310**, 536 (2007).
- [6] N. Hayashi, K. Wakabayashi, P. A. Frigeri, and M. Sigríst, Phys. Rev. B **73**, 092508 (2006).
- [7] S. Fujimoto, J. Phys. Soc. Jpn. **76**, 051008 (2007).
- [8] T. Yasuda, H. Shishido, T. Ueda, S. Hashimoto, R. Settai, T. Takeuchi, T. D. Matsuda, Y. Haga, and Y. Ōnuki, J. Phys. Soc. Jpn. **73**, 1657 (2004).
- [9] T. Takeuchi, T. Yasuda, M. Tsujino, H. Shishido, R. Settai, H. Harima, and Y. Ōnuki, J. Phys. Soc. Jpn. **76**, 014702 (2007).
- [10] N. Kimura, K. Ito, K. Saitoh, Y. Umeda, H. Aoki, and T. Terashima, Phys. Rev. Lett. **95**, 247004 (2005).
- [11] Y. Okuda, Y. Miyauchi, Y. Ida, Y. Takeda, C. Tonohiro, Y. Oduchi, T. Yamada, N. D. Dung, T. D. Matsuda, Y. Haga, T. Takeuchi, M. Hagiwara, K. Kindo, H. Harima, K. Sugiyama, R. Settai, and Y. Ōnuki, J. Phys. Soc. Jpn. **76**, 044708 (2007).
- [12] R. Settai, Y. Miyauchi, T. Takeuchi, F. Lévy, I. Sheikin, and Y. Ōnuki, J. Phys. Soc. Jpn. **77**, 073705 (2008).
- [13] R. Settai, I. Sugitani, Y. Ōnuki, T. D. Matsuda, Y. Haga, and H. Harada, Int. J. Mod. Phys. B **21**, 3238 (2007).
- [14] H. Q. Yuan, D. F. Agterberg, N. Hayashi, P. Badica, D. Vandervelde, K. Togano, M. Sigríst, and M. B. Salamon, Phys. Rev. Lett. **97**, 017006 (2006).
- [15] E. Bauer, G. Rogl, X.-Q. Chen, R. T. Khan, H. Michor, G. Hilscher, E. Royanian, K. Kumagai, D. Z. Li, Y. Y. Li, R. Podloucky, and P. Rogl, Phys. Rev. B **82**, 064511 (2010).
- [16] S. Oikawa, M. Nohara, and H. Takagi, presented at the 63<sup>rd</sup> JPS fall meeting, 23pQC (2008).
- [17] G. Eguchi, D. C. Peets, M. Kriener, Y. Maeno, E. Nishibori, Y. Kumazawa, K. Banno, S. Maki, and H. Sawa, Phys. Rev. B **83**, 024512 (2011).
- [18] G. Eguchi, F. Kneidinger, L. Salamakha, S. Yonezawa, Y. Maeno, and E. Bauer, J. Phys. Soc. Jpn. **81**, 074711 (2012).
- [19] K. Schwarz and P. Blaha, Comput. Mater. Sci. **28**, 259 (2003).
- [20] K. Momma and F. Izumi, J. Appl. Crystallogr. **44**, 1272 (2011).
- [21] K. Kihou, T. Saito, S. Ishida, M. Nakajima, Y. Tomioka, H. Fukazawa, Y. Kohori, T. Ito, S. Uchida, A. Iyo, C.-H. Lee, and H. Eisaki, J. Phys. Soc. Jpn. **79**, 124713 (2010).
- [22] K. Kobayashi, Nucl. Instrum. Methods. Phys. Res. A **601**, 32 (2009).
- [23] J. Kaczkowski and A. Jezierski, J. Alloys Compd. **509**, 6142 (2011).
- [24] H. Wadati, D. Kobayashi, H. Kumigashira, K. Okazaki, T. Mizokawa, A. Fujimori, K. Horiba, M. Oshima, N. Hamada, M. Lippmaa, M. Kawasaki, and H. Koinuma, Phys. Rev. B **71**, 035108 (2005).
- [25] T. Jeong, Solid State Commun. **150**, 337 (2010).
- [26] W. L. McMillan, Phys. Rev. **167**, 331 (1968).

- [27] D. U. Gubser and R. J. Soulen, J. Low Temp. Phys. **13**, 211 (1973).
- [28] J. Noffke and L. Fritsche, J. Phys. F – Metal Physics **12**, 921 (1982).
- [29] B. Mühlischlegel, Z. Physik. **155**, 313 (1959).
- [30] E. Helfand, N. R. Werthamer, and P. C. Hohenberg, Phys. Rev. **147**, 295 (1966).
- [31] H. Mukuda, S. Nishide, A. Harada, K. Iwasaki, M. Yogi, M. Yashima, Y. Kitaoka, M. Tsujino, T. Takeuchi, R. Settai, Y. Ōnuki, E. Bauer, K. M. Itoh, and E. E. Haller, J. Phys. Soc. Jpn. **78**, 014705 (2009).
- [32] C. Iniotakis, S. Fujimoto, and M. Sigrist, J. Phys. Soc. Jpn. **77**, 083701 (2008).
- [33] P. Fulde and R. A. Ferrell, Phys. Rev. **135**, A550 (1964).
- [34] Y. Matsunaga, N. Hiasa, and R. Ikeda, Phys. Rev. B **78**, 220508 (2008).